

We are IntechOpen, the world's leading publisher of Open Access books Built by scientists, for scientists

6,900

Open access books available

186,000

International authors and editors

200M

Downloads

Our authors are among the

154

Countries delivered to

TOP 1%

most cited scientists

12.2%

Contributors from top 500 universities



WEB OF SCIENCE™

Selection of our books indexed in the Book Citation Index
in Web of Science™ Core Collection (BKCI)

Interested in publishing with us?
Contact book.department@intechopen.com

Numbers displayed above are based on latest data collected.
For more information visit www.intechopen.com



Bandgap-Engineered Iron Oxides for Solar Energy Harvesting

Munetoshi Seki

Additional information is available at the end of the chapter

<http://dx.doi.org/10.5772/intechopen.73227>

Abstract

Epitaxial films of Rh-substituted $\alpha\text{-Fe}_2\text{O}_3$ were fabricated by a pulsed laser deposition technique, and their photoelectrochemical characteristics were investigated for the development of visible light-responsive photoanodes for water splitting. The photocurrent in the films upon irradiation in the visible region was significantly enhanced after Rh substitution. Moreover, a near-infrared photocurrent was clearly observed for Rh: Fe_2O_3 photoanodes, whereas no photoresponse could be detected for the $\alpha\text{-Fe}_2\text{O}_3$ films. These improved photoelectrochemical properties are attributed to the increased light absorption due to the hybridization of Rh-4*d* states and O-2*p* states at the valence band maximum. Moreover, Rh substitution also strongly influences the photocarrier transport properties of the films. The electrical conductivity of Rh: Fe_2O_3 is higher than that for $\alpha\text{-Fe}_2\text{O}_3$ by two orders of magnitude, which is possibly due to the extended 4*d* orbitals of the Rh³⁺ ions. Thus, the improved electrical properties may lead to an increased photocurrent by lowering the recombination rate of photogenerated carriers.

Keywords: solar water splitting, pulsed laser deposition, photoelectrochemical cell, iron oxides, bandgap engineering

1. Introduction

Iron oxides are well known to have various physical properties depending on their composition and crystal structures (see **Table 1**). They have been the subject of extensive investigation over the past decades from both fundamental and practical perspectives. For example, magnetite (Fe_3O_4) has been one of the most widely investigated oxides in various research fields owing to its high magnetic transition temperature ($\sim 585^\circ\text{C}$) and high spin polarization of carriers [1–3]. Numerous Fe_3O_4 -based ferromagnetic semiconductors and related spintronics

Composition (crystal structure)	ρ (Ωcm at 300 K)	T_N (K)	E_g (eV)	Physical properties	Refs.
$\alpha\text{-Fe}_2\text{O}_3$ (corundum)	$\sim 3 \times 10^{-3}$	950	2.1–2.2	Photoelectrochemical response to visible light	21–23
Fe_3O_4 (spinel)	$\sim 1 \times 10^{-2}$	860	–	Half metallicity	1–3
FeO (rock salt)	$\sim 3 \times 10^{-2}$	195	2.4–2.5	P-type semiconductor	4–6
BiFeO_3 (perovskite)	–	~ 640	2.3–2.1	Multiferroicity, Photo-voltaic effect	7–10
RFe_2O_4 (2D triangular)	$\sim 5 \times 10^2$	~ 230	–	Multiferroicity (charge-order-type)	11–14
$\text{R}_3\text{Fe}_5\text{O}_{12}$ (garnet)	–	~ 600	2.7–3.0	Giant magneto-optical effects	15–18
$\text{MFe}_{12}\text{O}_{19}$ (magnetoplumbite)	–	~ 700	–	Hard magnetic material	19, 20

Table 1. Various types of iron oxide and their physical properties (ρ : electrical resistivity, T_N : Néel temperature, and E_g : bandgap energy).

devices have been reported. Another simple iron oxide, wüstite (FeO) has attracted much attention in various fields such as Earth sciences, oxide electronics, spintronics, and chemical engineering [4–6]. Moreover, multifunctional bismuth ferrite (BiFeO_3 , BFO) has been of great interest owing to its potential applications in numerous room temperature multiferroic devices [7–9]. BFO is also considered to be a good candidate for use in solar energy conversion systems because of its electrical polarization-induced photovoltaic effects [10]. The triangular antiferromagnet RFe_2O_4 ($\text{R} = \text{Ho}, \text{Y}, \text{Yb}, \text{Lu}, \text{and In}$) is a multilayered oxide and was discovered in the 1970s by Kimizuka et al. [11]. RFe_2O_4 is composed of alternating hexagonal Fe–O and R–O layers stacked along the c -axis, and $\text{Fe}^{2+}/\text{Fe}^{3+}$ charge order occurs in the Fe–O layers below 320 K, which is followed by magnetic ordering below ~ 240 K [12]. Recently, a number of studies on RFe_2O_4 have been stimulated by the discovery of the giant magnetoelectric response in LuFe_2O_4 and its application to multiferroic devices is currently the subject of extensive investigations [13, 14]. A great number of investigations on the magneto-optical (MO) properties of garnet-type ferrites ($\text{R}_3\text{Fe}_5\text{O}_{12}$) have been carried out for applications in the field of optical communications. They are currently recognized as the most promising materials in magnonics and related areas. Especially, they are widely used in ferromagnetic resonance experiments and magnon-based Bose-Einstein-condensates owing to their extremely low damping [15–18]. Furthermore, there has been much interest in hexaferrites, $\text{MFe}_{12}\text{O}_{19}$ ($\text{M} = \text{Ba}$ and Sr) [19, 20], which are commonly applied in a wide variety of data storage and recording devices. One of the most favorable characteristics of the above iron oxides is their chemical stability, and they are also nontoxic. Moreover, iron and oxygen are abundant in the Earth. These features imply that iron oxides are favorable materials for applications in environmentally friendly electronics, spintronics, and magnonics. The author focuses on $\alpha\text{-Fe}_2\text{O}_3$ commonly referred as a hematite, which is known as a promising candidate for semiconductor photoanodes for pho

photoelectrochemical (PEC) water splitting [21–23]. A schematic of a PEC cell is shown in **Figure 1**. They consist of a photoactive electrode and a metal counter electrode immersed in a suitable electrolyte solution. The photogenerated electron-hole pairs are split by the electric field in the space-charge region at the surface of photoelectrodes. Since Honda and Fujishima's pioneered work on PEC water splitting with a TiO_2 photoelectrode [24], there has been worldwide research focused on the solar generation of hydrogen as a renewable and clean energy source. Many kinds of materials including TiO_2 have been investigated for their application as photoelectrodes. However, most of them are wide-gap semiconductors, and only a small fraction of the solar spectrum can be utilized by the PEC cells based on these materials. A high PEC responsivity to visible (VIS) and near-infrared (near-IR) light is required to harvest the lower energy region of the solar spectrum. From this viewpoint, $\alpha\text{-Fe}_2\text{O}_3$ has attracted much attention because of its promising properties for application as a photoanode in a solar water splitting cell. It possesses a narrow bandgap energy (E_g) of 2.1 eV that allows for the absorption of up to 40% of solar spectrum. However, the reported efficiencies for PEC water splitting using $\alpha\text{-Fe}_2\text{O}_3$ -based photoelectrodes are significantly low. This poor PEC property of $\alpha\text{-Fe}_2\text{O}_3$

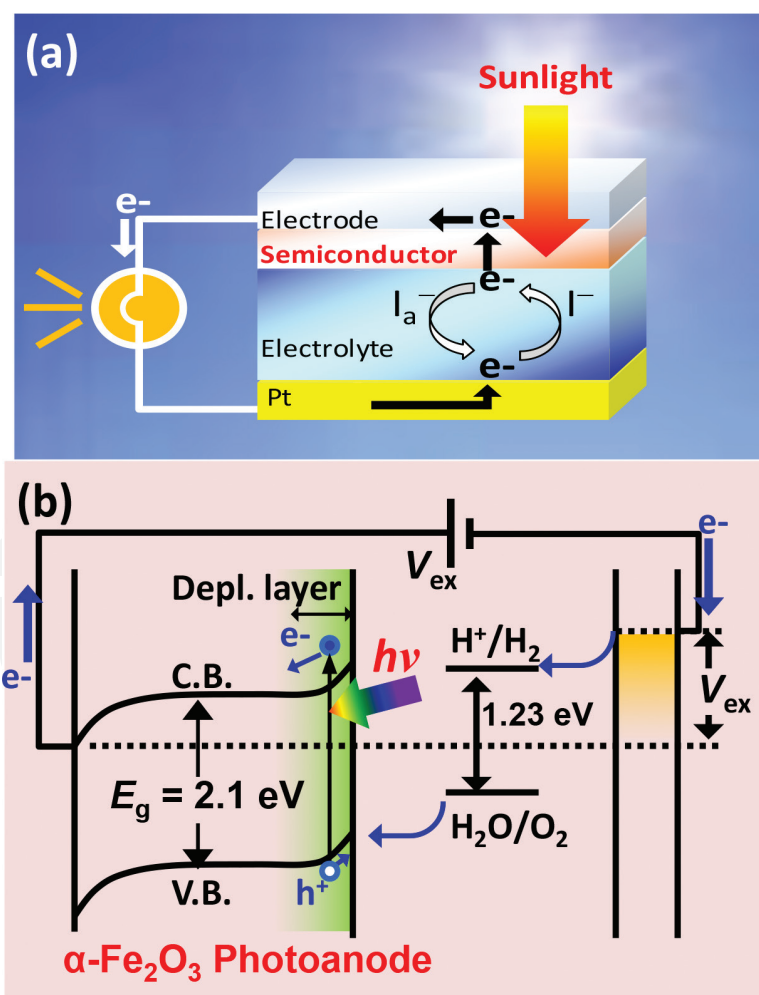


Figure 1. (a) Schematic of the photoelectrochemical (PEC) cell for solar water splitting and (b) electronic band structure of the PEC cell. Adapted by permission from Springer: *Correlated Functional Oxides* edited by H. Nishikawa, N. Iwata, T. Endo, Y. Takamura, G. Lee, and P. Mele (2017).

can be attributed to the short diffusion length of the photogenerated holes. For $\alpha\text{-Fe}_2\text{O}_3$ -based PEC cells, only the holes generated near the electrolyte/photoanode interface can oxidize water [25, 26]. That is, most of the photogenerated electron-hole pairs recombine before reaching the photoelectrode surface. The hematite lattice is composed of an alternating stack of Fe bilayers and O layers along c-axis as illustrated in **Figure 2**. Spins of Fe^{3+} ions within each bilayer are parallel, whereas adjacent Fe bilayers have opposite spins. 3d electrons of Fe can move by hopping via the change in the $\text{Fe}^{2+}/\text{Fe}^{3+}$ valence within the Fe bilayers, whereas the exchange of electrons between neighboring Fe bilayers is spin forbidden [27–29]. Therefore, the orientation of a highly conducting (001) plane vertical to the substrate will facilitate the collection of photogenerated carriers and suppress their recombination. The author employed a Ta-doped SnO_2 (TTO) layer grown on $\alpha\text{-Al}_2\text{O}_3$ (110) single-crystal substrates for the epitaxial growth of $\alpha\text{-Fe}_2\text{O}_3$ films along the [110] direction. As shown in **Figure 3(a)**, the SnO_2 (101) plane matches the $\alpha\text{-Fe}_2\text{O}_3$ (110) plane with a lattice mismatch of approximately 1.3%, which is favorable for the epitaxial growth of hematite along the [110] direction on the $\text{SnO}_2(101)/\alpha\text{-Al}_2\text{O}_3(101)$ substrate [30]. Another issue regarding $\alpha\text{-Fe}_2\text{O}_3$ concerns its low responsivity to near-IR light. It is well known that the photocurrent in $\alpha\text{-Fe}_2\text{O}_3$ is maximized at a wavelength (λ) of ~ 350 nm, exhibits a significant decrease with increasing λ , and approaches zero at approximately 600 nm, corresponding to its bandgap [31]. An improvement of the PEC responsivity in VIS and near-IR regions by controlling the bandgap would be useful for solar energy harvesting. Unfortunately, there exist few reports on such bandgap engineering in $\alpha\text{-Fe}_2\text{O}_3$. From this viewpoint, the author focused on Rh-substituted $\alpha\text{-Fe}_2\text{O}_3$ (FRO). $\alpha\text{-Rh}_2\text{O}_3$ has a bandgap E_g of

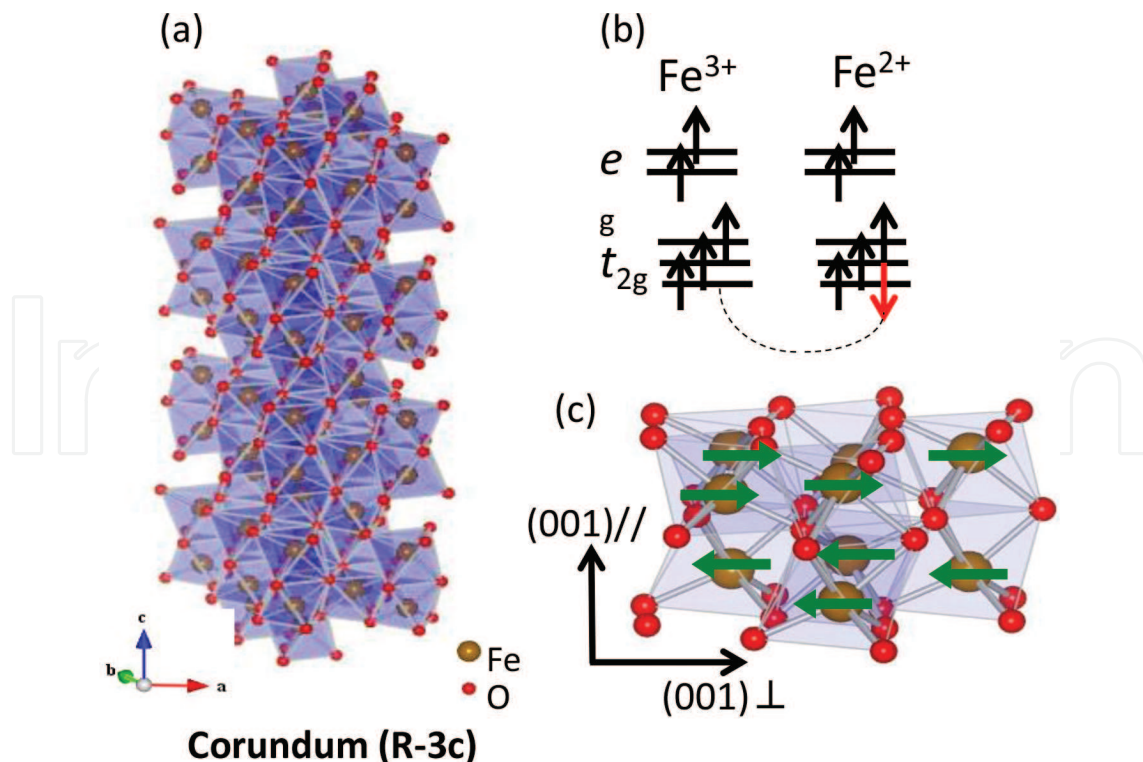


Figure 2. (a) Corundum-type crystal structure of $\alpha\text{-Fe}_2\text{O}_3$. (b) The transport of electron in the Fe 3d band is schematically illustrated. (c) Antiferromagnetic spin coupling in $\alpha\text{-Fe}_2\text{O}_3$. [Copyright (2014), The Japan Society of Applied Physics].

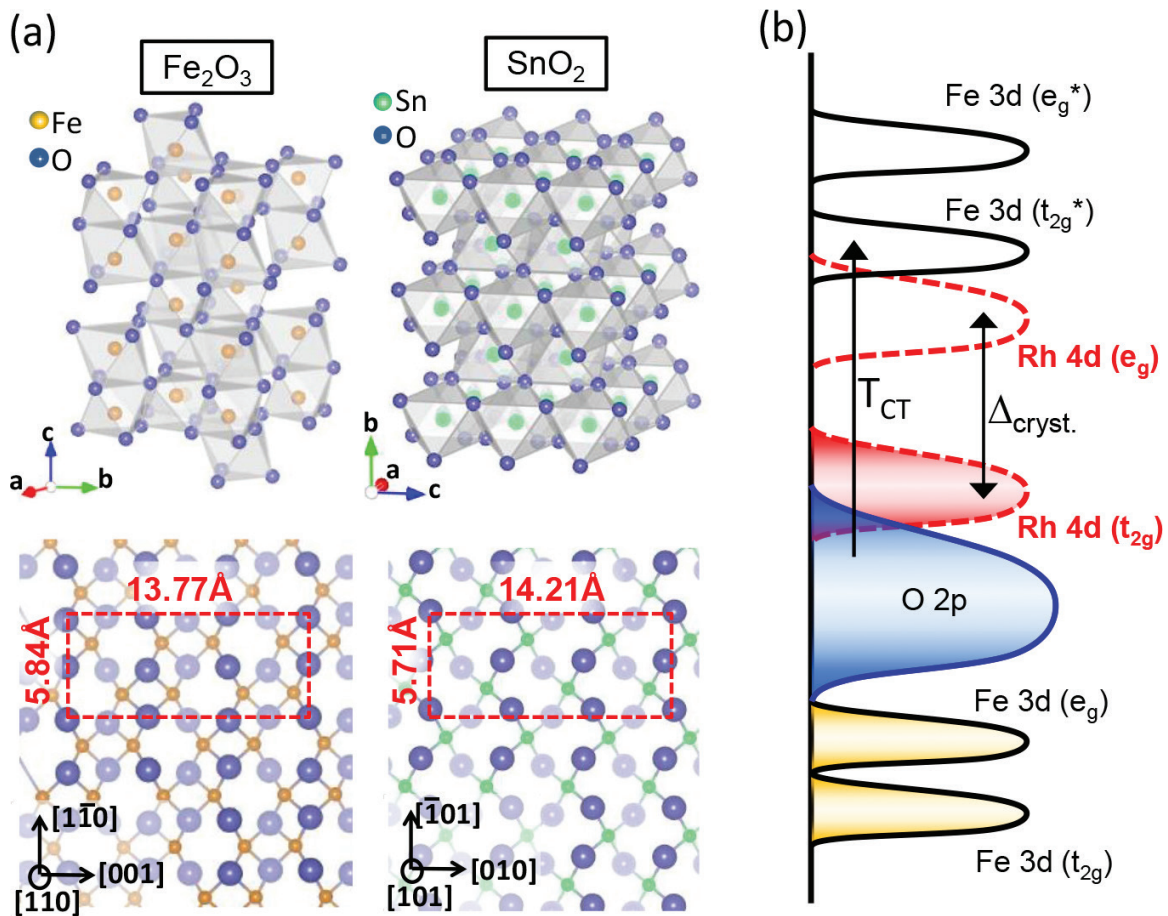


Figure 3. (a) Top: Crystal structures of $\alpha\text{-Fe}_2\text{O}_3$ (corundum type) and SnO_2 (rutile type). Bottom: Schematic showing the in-plane atomic configuration of $\alpha\text{-Fe}_2\text{O}_3$ and SnO_2 . [Copyright (2012), The Japan Society of Applied Physics].

1.2–1.4 eV [32] and the same corundum-type crystal structure as $\alpha\text{-Fe}_2\text{O}_3$. Therefore, the bandgap of $\alpha\text{-Fe}_2\text{O}_3$ could be narrowed by Rh substitution in the films [33, 34]. **Figure 3(b)** shows a schematic of the band alignment of FRO [35, 36]. $\alpha\text{-Fe}_2\text{O}_3$ is a charge transfer-type insulator with a bandgap between the Fe 3d state (upper Hubbard band) and the fully occupied O 2p state. In contrast, the bandgap of $\alpha\text{-Rh}_2\text{O}_3$ originates from the ligand field splitting of the Rh 4d orbitals. The Rh 4d (t_{2g}) band in $\alpha\text{-Rh}_2\text{O}_3$ lies near the O 2p band, and they effectively hybridize at the valence band maximum (VBM) [32, 37, 38]. In this chapter, the PEC characteristics of FRO photoanodes fabricated using pulsed laser deposition (PLD) are discussed in association with their electronic structures.

2. Experimental procedures

The FRO films were grown using a PLD technique with an argon fluoride (ArF) excimer laser ($\lambda = 193\text{ nm}$). The laser pulse frequency was 5 Hz. The fluence remained constant at 1.1 J/cm^2 . The typical growth rate of the films was 0.5 nm/min . After deposition, the FRO films were annealed in air at 700°C to improve their crystallinity. The author employed two types of

bottom electrodes, viz., TTO deposited onto an α - Al_2O_3 (110) substrate and polycrystalline fluorine-doped SnO_2 (FTO) formed on a soda-lime glass substrate. An $\text{Fe}_{2-x}\text{Rh}_x\text{O}_3$ ($x = 0.0$ – 2.0) pellet prepared by a solid-state reaction was used as a target for PLD. The growth temperature was kept at 700 and 800°C for the FRO and TTO films, respectively. The crystal structures of the samples were confirmed using X-ray diffraction (XRD). In the PEC measurement, the I - V properties were measured using an electrochemical analyzer under the illumination of Xe lamp (500 W). Optical measurements were conducted using a Vis-UV spectrometer. X-ray photoemission spectroscopy (XPS) was performed to evaluate the structure of the valence band (VB) in the FRO films.

3. Crystal structures

The XRD 2 theta-omega scan of the FeRhO_3 films is shown in **Figure 4(a)**. For the as-deposited sample, broad peaks are observed at 35 and 75°, which are ascribed to the (110) and (220)

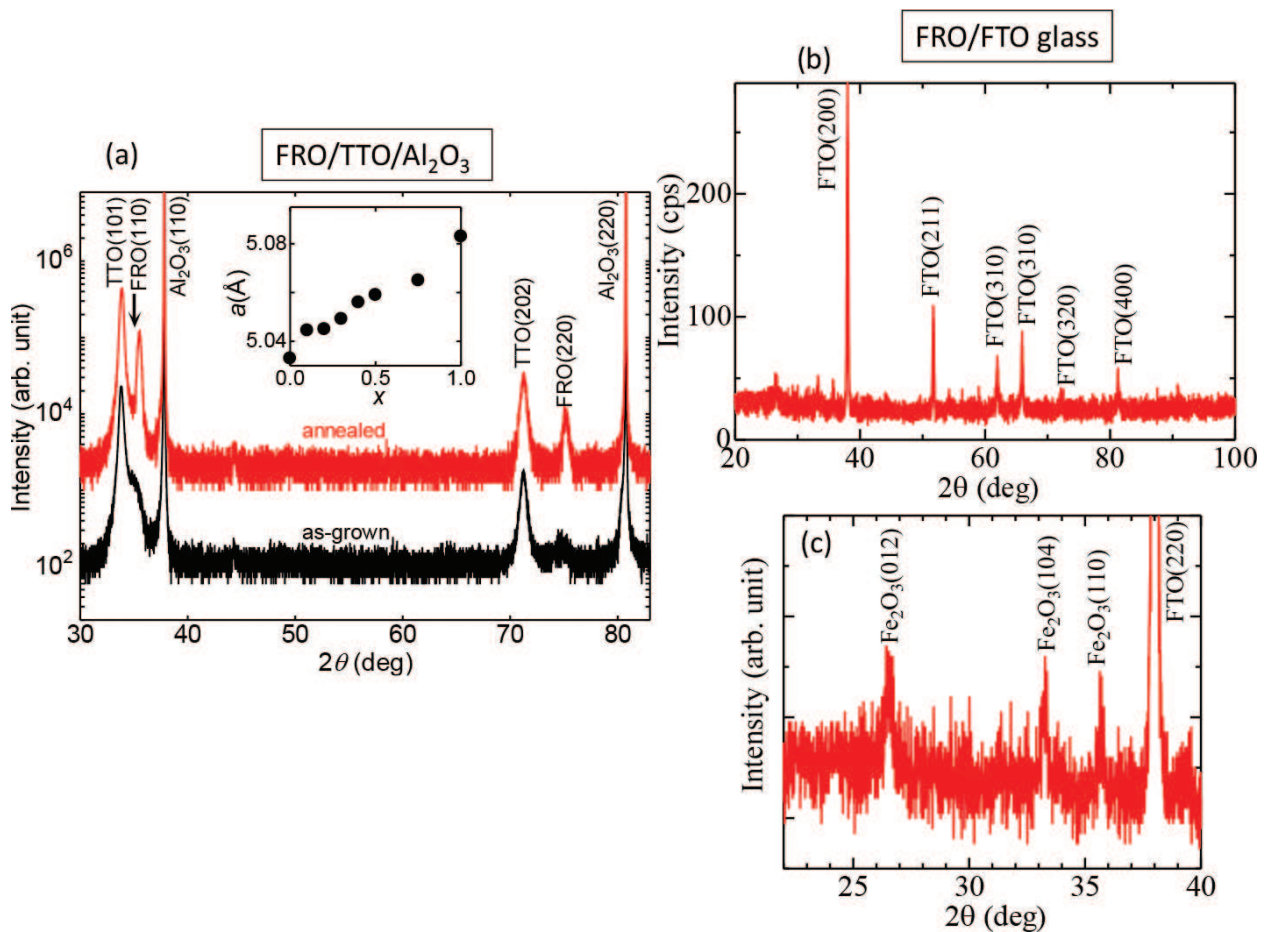


Figure 4. (a) XRD $2\theta/\omega$ scan of the FRO film ($x = 1.0$) grown on TTO/ α - Al_2O_3 (110). (b) XRD pattern of the FRO film ($x = 0.2$) grown on the FTO substrate. (c) Magnified image of the XRD pattern of (b). [Copyright (2012 and 2014), The Japan Society of Applied Physics].

reflections of corundum-type FRO, respectively. This indicates that the films grown along [110] despite their low crystalline quality. Sharp peaks appear after thermal annealing, suggesting an improvement in the crystallinity. The in-plane epitaxial relationship was evaluated to be TTO [010]//FRO [001] by in-plane XRD measurements. This result agrees with the atomic configurations in **Figure 3(a)** [30]. The lattice constants obey Vegard's law, implying that Fe had been appropriately substituted with Rh. In contrast to the films deposited onto the sapphire substrates, the films deposited on the glass substrates are polycrystalline in nature, as shown in **Figure 4(b)** and **(c)**.

4. Optical properties

Figure 5(a) shows the light absorption spectra of the films. The fundamental absorption edge of $\alpha\text{-Fe}_2\text{O}_3$ is related to charge transfer from O 2p states to the upper Hubbard band promoted by photons [denoted by T_{CT} in **Figure 3(b)**]. For films with a higher Rh content, a broadband appears at 1.5–4.5 eV that is possibly related to $\alpha\text{-Rh}_2\text{O}_3$. The optical transition in $\alpha\text{-Rh}_2\text{O}_3$ is unclear; its absorption edge is considered to be associated with the $d-d$ transition of Rh^{3+} , judging from the bandgap structure [31, 39]. **Figure 5(b)** shows the values of an indirect bandgap (E_g), which were derived from the Tauc relation, $\alpha h\nu \propto (h\nu - E_g)^2$ (α : optical absorption coefficient and $h\nu$: photon energy). E_g decreases as the content of Rh in the films increases according to the above discussion. Value of E_g of 2.1 and 1.2 eV were obtained for $\alpha\text{-Fe}_2\text{O}_3$ and $\alpha\text{-Rh}_2\text{O}_3$, respectively. These values are almost identical to those reported for polycrystalline films [40].

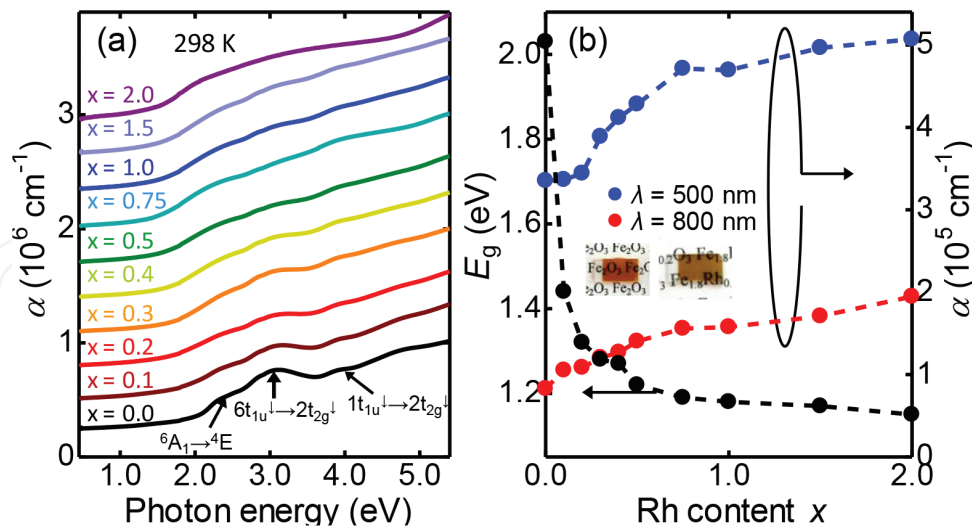


Figure 5. (a) Optical absorption coefficients as a function of the wavelength for FRO films on $\alpha\text{-Al}_2\text{O}_3(110)$ substrate at 298 K. For clarity, each spectrum is offset, with a spacing scaled to the composition. The peaks of $\alpha\text{-Fe}_2\text{O}_3$ ($x = 0.0$) are assigned according to Ref. 19. (b) Compositional dependence of the indirect bandgap energy E_g and the absorption coefficients α at $\lambda = 500$ and 800 nm. The photographs of $\alpha\text{-Fe}_2\text{O}_3$ ($x = 0.0$) and FRO ($x = 0.2$) films are inset. [Copyright (2012), The Japan Society of Applied Physics].

5. XPS spectroscopy

The results of XPS are presented in **Figure 6**. In the spectra of Fe $2p$ core level (**Figure 6(a)**), main peaks are at around 710 and 723 eV and are assigned to Fe $2p_{2/3}$ and $2p_{1/3}$ orbitals of α -Fe₂O₃, respectively [41–43]. These core level peaks become weaker as the Rh content increases. In turn, new distinct peaks appear at approximately 310 and 315 eV, which are assigned to Rh $3d_{3/2}$ and $3d_{5/2}$ orbitals, respectively [44, 45]. As seen in **Figure 6(c)**, the VBM of α -Fe₂O₃ is estimated to be 0.65 eV. In contrast, the VBM of α -Rh₂O₃ is located near the Fermi level (\sim 0.0 eV). Three distinct peaks are observed in the VB spectrum of the films. The bands centered at 1, 2, and 3 eV in the VB spectrum of α -Fe₂O₃ are assigned to the Fe $3e_g$, $2t_g$, and $2e_g$ orbitals, respectively [46]. The crystal field splitting energy between the Fe $3e_g$ and $2t_g$ orbitals was estimated to be 2.5 eV in a previous study [47], which agrees with the experimental value (2.4 eV) well. In the VB spectrum of α -Rh₂O₃, three distinct peaks similarly appear. Unfortunately, there are

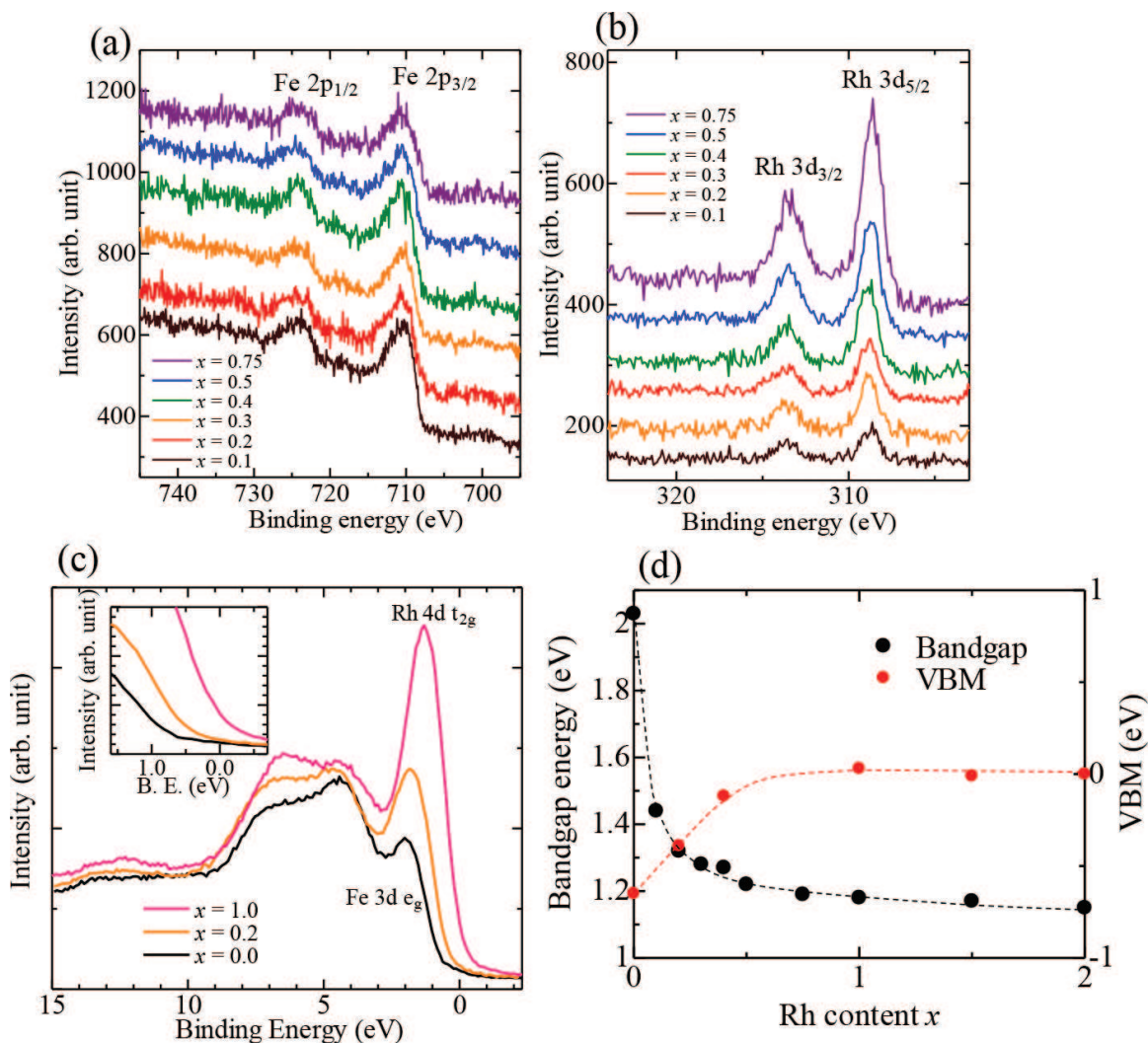


Figure 6. XPS spectra of (a) Fe $2p$ and (b) Rh $3d$ core levels for FRO films. (c) Valence band XPS spectra of FRO films. The inset shows the enlarged VB spectra near the Fermi level. (d) Compositional dependence of VBM and bandgap energy. [Copyright (2012), The Japan Society of Applied Physics].

hardly any reports of VB spectra for α - Rh_2O_3 . However, by comparing with results obtained by ultraviolet photoemission spectroscopy (UPS) for ZnRh_2O_4 [48, 49], the peak observed at 1 eV is attributed to the t_{2g} orbitals of the RhO_6 octahedra in α - Rh_2O_3 . The peaks at 2 and 3 eV are assigned to the Rh $4d$, $5s$, and $5p$ mixed states [48]. The VBM and E_g exhibit a similar dependences on the Rh content, as shown in **Figure 6(d)**. In addition, the change in the VBM (0.7 eV) for $x = 1.0$ is close to the bandgap decrease (0.8 eV) for $x = 1.0$. From these results, we can conclude that the bandgap decrease by Rh substitution is due to the hybridization of the O $2p$ valence band with the Rh t_{2g} band at the VBM.

6. Photoelectrochemical properties

The current-potential curves of the films are shown in **Figure 7(a)** and **(b)**. For α - Fe_2O_3 , the photocurrent is $2.87 \mu\text{A}/\text{cm}^2$ at 0.5 V under irradiation with VIS light ($\lambda = 400\text{--}700 \text{ nm}$). As shown in **Figure 7(a)**, the VIS photocurrent is remarkably increased after Rh substitution ($17.3 \mu\text{A}/\text{cm}^2$ at 0.5 V for $x = 0.2$). The effect of Rh substitution becomes more obvious with near-IR irradiation

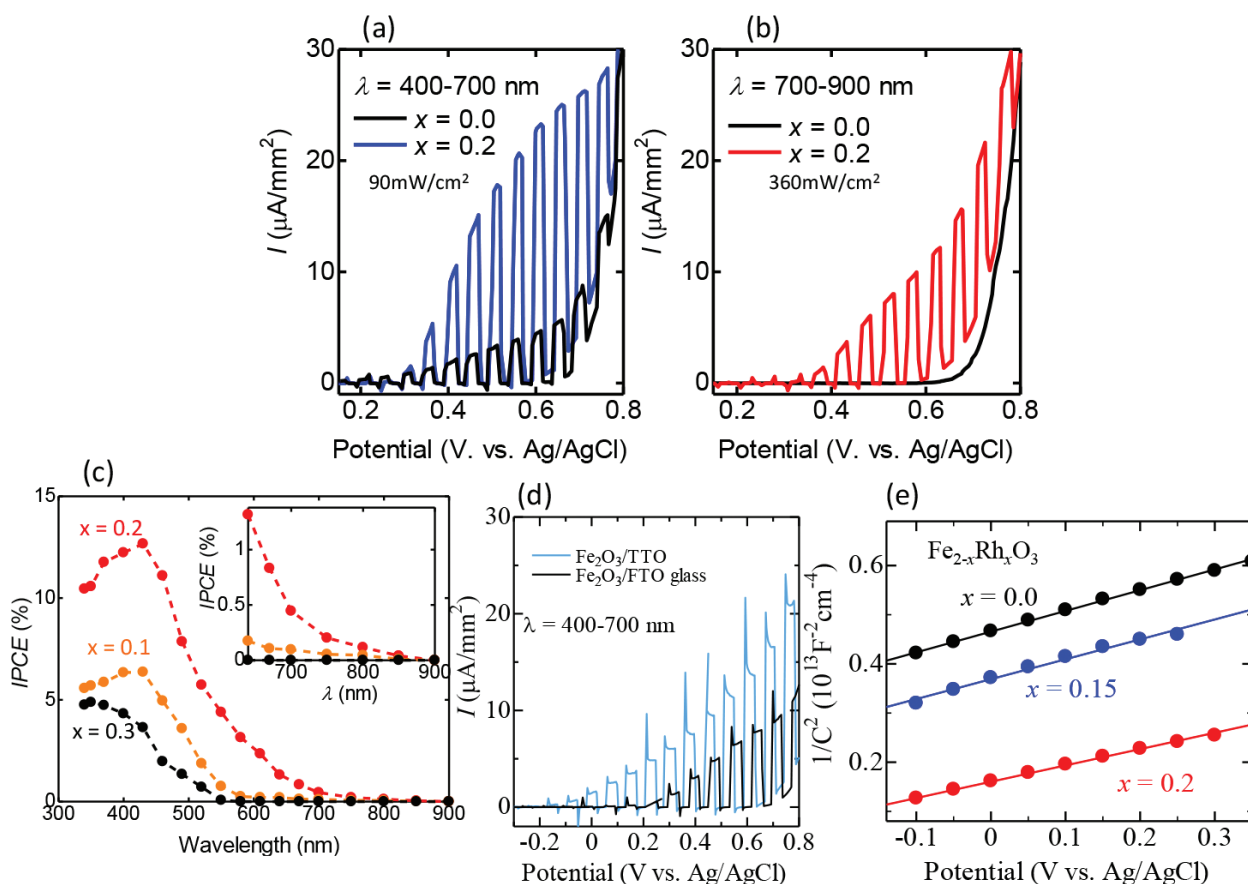


Figure 7. Chopped I - V curves under illumination with (a) VIS light ($\lambda = 400\text{--}700 \text{ nm}$, $100 \text{ mW}/\text{cm}^2$) and (b) NIR light ($\lambda = 700\text{--}900 \text{ nm}$, $640 \text{ mW}/\text{cm}^2$) for $x = 0.0$ and 0.2 . (c) IPCE as a function of wavelength for the FRO films at 0.55 V vs. Ag/AgCl in an aqueous electrolytic solution containing 1.0 M NaOH . The inset shows the magnified IPCE spectra at $\lambda = 600\text{--}900 \text{ nm}$ (d) I - V curves of α - Fe_2O_3 films deposited on $\text{TTO}/\alpha\text{-Al}_2\text{O}_3(110)$ (blue) and FTO glass (black) substrates. (e) Mott-Schottky plots for FRO films. [Copyright (2012 and 2014), The Japan Society of Applied Physics].

($\lambda = 700\text{--}900\text{ nm}$). As shown in **Figure 7(b)**, for $x = 0.2$, a near-IR photocurrent is evidently observed, whereas a photocurrent is hardly detected for the $\alpha\text{-Fe}_2\text{O}_3$ film. These improved PEC properties of the FRO films may be caused by the increased light absorption in these wavelength regions. Furthermore, the electrical properties of the films also affect their PEC performance. The electrical conductivity for $x = 0.2$ ($\sigma = 3.8 \times 10^{-4}\ \Omega^{-1}\ \text{cm}^{-1}$ at 300 K) is significantly larger than that for $x = 0.0$ ($\sigma = 2.6 \times 10^{-6}\ \Omega^{-1}\ \text{cm}^{-1}$ at 300 K). This is possibly due to the extended profile of the Rh $4d$ state [50]. Thus, the improved electrical conductivity possibly causes an increased photocurrent by lowering the recombination rate of the photocarriers as in the case for Ti- or Si-doped $\alpha\text{-Fe}_2\text{O}_3$ [22, 38, 40]. In **Figure 7(c)**, the spectra of the incident photon-to-current efficiency (IPCE) are shown. The IPCE was estimated using the following relationship: $IPCE (\%) = 100 \times [hc/e] \times I/[P \times \lambda]$, where h , c , e , I (mA/cm^2), and P (mW/cm^2) denote the Planck constant, the light velocity, the elementary charge, the photocurrent, and the power of the illumination per unit area, respectively [22]. The IPCE for $x = 0.1$ and 0.2 is much higher than that of $\alpha\text{-Fe}_2\text{O}_3$ in the $340\text{--}850\text{ nm}$ wavelength region. For $\alpha\text{-Fe}_2\text{O}_3$, the IPCE decreases to zero when the wavelength exceeds 610 nm , corresponding to its bandgap. On the other hand, for $x = 0.2$, the IPCE is 2.35% at 610 nm and gradually decreased to 0.11% at 850 nm as shown in the inset of **Figure 7(c)**. The IPCE decreases drastically when x exceeds 0.2 as shown in **Figure 7(c)**, and a photocurrent is hardly detected for $x \geq 0.75$ in the $340\text{--}900\text{ nm}$ wavelength region. These results possibly reflect the drastic change in the optical transition process caused by Rh substitution. On the one hand, the photogenerated carriers in $\alpha\text{-Fe}_2\text{O}_3$ diffuse through the bands related to the Fe $3d$ and O $2p$ states [22]. On the other hand, the recombination probability of the carriers generated in $\alpha\text{-Rh}_2\text{O}_3$ following the $d\text{-}d$ transition in Rh^{3+} is significantly high [32, 51]. This nature impairs the PEC performance for a higher Rh content. We note that the rate of decrease in E_g is drastically decreased when x exceeds 0.2 . This result suggests that the band-edge electronic structure is not strongly influenced by Rh substitution; therefore, the $d\text{-}d$ transition predominantly occurs for $x > 0.2$. The IPCE peak wavelength shifts from 350 to 430 nm as Rh content increases from $x = 0.0$ to 0.2 . This is a desirable feature for energy harvesting, because the peak of the solar spectrum is at $\sim 475\text{ nm}$. The PEC properties of the polycrystalline film ($x = 0.2$) are shown in **Figure 7(d)**. The photocurrent of the single-crystal FRO grown on a $\text{TTO}/\text{Al}_2\text{O}_3$ (110) substrate is higher than that of the polycrystalline FRO grown on FTO glass. This result can be explained by the electronic transport properties of the films. The conductivity of the (110)-oriented single-crystalline film along the out-of-plane direction ($\sigma = 3.4 \times 10^{-4}\ \Omega^{-1}\ \text{cm}^{-1}$) is much larger than that of the polycrystalline film ($\sigma = 8.8 \times 10^{-6}\ \Omega^{-1}\ \text{cm}^{-1}$). The improvement (σ) in the electrical conductivity in the single-crystal films may accelerate the collection of photocarriers, resulting in their enhanced PEC properties. In **Figure 7(e)**, the Mott-Schottky plots are shown. The density of donors N is expressed as follows:

$$N = [2/(e_0 \varepsilon_0 \varepsilon)] [d(1/C^2)/dV]^{-1} \quad (1)$$

where e_0 represents an electron charge, and ε_0 and ε are the vacuum and relative electric permittivities, respectively. By employing the reported value of $\varepsilon = 80$ for hematite, the donor densities are calculated to be 4.2×10^{17} ($x = 0.2$) and $5.3 \times 10^{17}\ \text{cm}^{-3}$ for $x = 0.0$ (hematite) and 0.2 , respectively. Thus, the donor density does not significantly change after Rh substitution, in contrast to the case for Ti- or Si-doped $\alpha\text{-Fe}_2\text{O}_3$. It is considered that the number of Fe^{2+} ions, which acts as electron donors, increases when Fe^{3+} is substituted with Ti^{4+} or Si^{4+} owing to the charge neutrality. In

contrast, in the FRO films, the valence of the Rh ions is +3, and hence, the content of Fe^{2+} does not increase after Rh substitution. Nevertheless, the conductivity for $x = 0.2$ is two orders of magnitude larger than that for $x = 0.0$. Therefore, it is considered that the carrier mobility is remarkably increased after Rh substitution probably owing to the extended nature of the Rh $4d$ states.

7. Summary

The Rh-substituted $\alpha\text{-Fe}_2\text{O}_3$ photoelectrodes were successfully fabricated using a pulsed laser deposition method. Their bandgap narrowed as the Rh content increased. XPS analyses revealed that the bandgap narrowing is brought by the hybridization of the Rh $4d$ state with the $\text{O}2p\text{-Fe}3d$ states at the VBM of $\alpha\text{-Fe}_2\text{O}_3$. The photocurrent was significantly enhanced for lower Rh contents. Moreover, the PEC properties were improved by the control of crystal growth condition. These results will be utilized in the development of high-efficiency solar energy conversion devices based on iron oxides.

Acknowledgements

This work was supported by JSPS Core-to-Core Program, A. Advanced Research Networks, and JSPS KAKENHI grant numbers JP16K14226 and JP15H03563. The author would like to thank Prof. H. Tabata, Prof. H. Matsui, and Dr. H. Yamahara for their support and helpful discussion.

Author details

Munetoshi Seki

Address all correspondence to: m-seki@ee.t.u-tokyo.ac.jp

Center for Spintronics Research Network (CSRN), Graduate School of Engineering,
The University of Tokyo, Tokyo, Japan

References

- [1] Bibes M, Berthelemy A. Oxide Spintronics. *IEEE Transactions on Electron Devices*. 2007;**54**:1003-1023. DOI: 10.1109/TED.2007.894366
- [2] Zhang Z, Satpathy S. Electron states, magnetism, and the Verwey transition in magnetite. *Physical Review B*. 1991;**44**:13319-13331. DOI: 10.1103/PhysRevB.44.13319
- [3] Seki M, Hossain AKM, Kawai T, Tabata H. High-temperature cluster glass state and photomagnetism in Zn and Ti-substituted NiFe_2O_4 films. *Journal of Applied Physics*. 2005; **97**:083541(1)-(6). DOI: 10.1063/1.1863422

- [4] Seki M, Takahashi M, Adachi M, Yamahara H, Tabata H. Fabrication and characterization of wüstite-based epitaxial thin films: p-Type wide-gap oxide semiconductors composed of abundant elements. *Applied Physics Letters*. 2014;**105**:113105(1)-(4). DOI: 10.1063/1.4896316
- [5] Bowen HK, Adler D, Auker BH. Electrical and optical properties of FeO. *Journal of Solid State Chemistry*. 1975;**12**:355-359. DOI: 10.1016/0022-4596(75)90340-0
- [6] Srinivasan G, Seehra MS. Variation of magnetic properties of Fe_xO with nonstoichiometry. *Journal of Applied Physics*. 1984;**55**:2327-2329. DOI: 10.1063/1.333651
- [7] Wang J, Neaton JB, Zheng H, Nagarajan V, Ogale SB, Liu B, Viehland D, Vaithyanathan V, Scholm DG, Waghmare UV, Spaldin NA, Rabe KM, Wutting M, Ramesh R. Epitaxial BiFeO_3 multiferroic thin film heterostructures. *Science*. 2003;**299**:1719-1722. DOI: 10.1126/science.1080615
- [8] Polomska M, Kaczmarek W, Pajak Z. Electric and magnetic properties of $(\text{Bi}_{1-x}\text{La}_x)\text{FeO}_3$ solid solutions. *Physica Status Solidi A*. 1974;**23**:567-574. DOI: 10.1002/pssa.2210230228
- [9] Sonowska I, Neumaier TP, Steichele E. Spiral magnetic ordering in bismuth ferrite. *Journal of Physics C: Solid State Physics*. 1982;**15**:4835-4846. DOI: 10.1088/0022-3719/15/23/020
- [10] Yang SY, Martin LW, Byrnes SJ, Conry TE, Basu SR, Paran D, Reichertz L, Ihlefeld J, Adamo C, Melville A, Chu Y-H, Yang C-H, Musfeldt JL, Sholm DG, Ager III JW, Ramesh R. Photovoltaic effects in BiFeO_3 . *Applied Physics Letters*. 2009;062909(1)-(3). DOI: 10.1063.1.3204695
- [11] Kimizuka N, Katsura T. Standard free energy of formation of YFeO_3 , $\text{Y}_3\text{Fe}_5\text{O}_{12}$, and a new compound YFe_2O_4 in the Fe- Fe_2O_3 - Y_2O_3 system at 1200°C. *Journal of Solid State Chemistry*. 1975;**13**:176-181. DOI: 10.1016/0022-4596(75)90116-4
- [12] Ikeda N, Ohsumi H, Ohwada K, Ishii K, Imai T, Kakurai K, Murakami Y, Yoshii K, Mori S, Horibe Y, Kito H. Ferroelectricity from ion valence ordering in the charge frustrated system LuFe_2O_4 . *Nature*. 2005;**436**:1136-1138. DOI: 10.1038/nature04039
- [13] Xiang HJ, Whangbo M-H. Charge order and the origin of giant magnetocapacitance in LuFe_2O_4 . *Physical Review Letters*. 2007;**98**:246403(1)-(4). DOI: 10.1103/PhysRevLett.98.246403
- [14] Seki M, Konya T, Inaba K, Tabata H. Epitaxial thin films of InFe_2O_4 and InFeO_3 with two-dimensional triangular lattice structures grown by pulsed laser deposition. *Applied Physics Express*. 2010;**3**:105801(1)-(3). DOI: 10.1143/APEX.3.105801
- [15] Kumar N, Kim NG, Park YA, Hur N, Jung JH, Ham KJ, Yee KJ. Epitaxial growth of terbium iron garnet thin films with out-of-plane axis of magnetization. *Thin Solid Films*. 2008;**516**:7753-7757. DOI: 10.1016/j.tsf.2008.05.032
- [16] Krockenberger Y, Matsui H, Hasegawa T, Kawasaki M, Tokura Y. Solid phase epitaxy of ferromagnetic $\text{Y}_3\text{Fe}_5\text{O}_{12}$ garnet thin films. *Applied Physics Letters*. 2008;**93**:092505(1)-(3). DOI: 10.1063/1.2976747

- [17] Yamahara H, Mikami M, Seki M, Tabata H. Epitaxial strain-induced magnetic anisotropy in $\text{Sm}_3\text{Fe}_5\text{O}_{12}$ thin films grown by pulsed laser deposition. *Journal of Magnetism and Magnetic Materials*. 2011;**323**:3143-3146. DOI: 10.1016/j.jmmm.2011.06.074
- [18] Adachi M, Seki M, Yamahara H, Tabata H. Long-term potentiation of magnonic synapses by photocontrolled spin current mimicked in reentrant spin-glass garnet ferrite $\text{Lu}_3\text{Fe}_{5-2x}\text{Co}_x\text{Si}_x\text{O}_{12}$ thin films. *Applied Physics Express*. 2015;**91**:085118(1)-(7). DOI: 10.7567/APEX.8.043002
- [19] Xu P, Han X, Wang M. Synthesis and magnetic properties of $\text{BaFe}_{12}\text{O}_{19}$ Hexaferrite nanoparticles by a reverse microemulsion technique. *Journal of Physical Chemistry C*. 2007;**111**:5866-5870. DOI: 10.1021/jp068955c
- [20] Zi ZF, Sun YP, Zhu XB, Yang ZR, dai JM, Song WH. Structural and magnetic properties of $\text{SrFe}_{12}\text{O}_{19}$ hexaferrite synthesized by a modified chemical co-precipitation method. *Journal of Magnetism and Magnetic Materials*. 2008;**320**:2746-2751. DOI: 10.1016/j.jmmm.2008.06.009
- [21] Chernomordik BD, Russell HB, Cvelbar U, Jasinski JB, Kumar V, Dautsch T, Sunkara MK. Photoelectrochemical activity of as-grown, $\alpha\text{-Fe}_2\text{O}_3$ nanowire array electrodes for water splitting. *Nanotechnology*. 2012;**23**:194009(1)-(9). DOI: 10.1088/0957-4484/23/19/194009
- [22] Kay A, Cesar I, Grätzel M. New benchmark for photooxidation by nanostructured $\alpha\text{-Fe}_2\text{O}_3$ films. *Journal of American Chemical Society*. 2006;**128**:15714-15721. DOI: 10.1021/ja0643801
- [23] Thimsen E, Formal FL, Grätzel M, Warren SC. Influence of plasmonic Au nanoparticles on the photoactivity $\alpha\text{-Fe}_2\text{O}_3$ electrodes for water splitting. *Nano Letters*. 2011;**11**:35-43. DOI: 10.1021/nl1022354
- [24] Fujishima A, Honda K. Electrochemical photolysis of water at a semiconductor electrode. *Nature*. 1972;**238**:37-38. DOI: 10.1038/238038a0
- [25] Sanchez C, Sieber KD, Somorjai GA. The photoelectrochemistry of niobium doped $\alpha\text{-Fe}_2\text{O}_3$. *Journal of Electroanalytical Chemistry and Interfacial Electrochemistry*. 1988;**252**:269-290. DOI: 10.1016/0022-0728(88)80216-X
- [26] Campbell AS, Schwertmann U, Stanjek H, Friedl J, Kyek A, Campbell PA. Si incorporation into hematite by heating Si-Fe ferrihydrite. *Langmuir*. 2002;**18**:7804-7809. DOI: 10.1021/la011741w
- [27] Benjelloun D, Bonnet J-P, Doumerc J-P, Launay J-C, Onillon M, Hagenmuller P. Anisotropie des proprietes electriques de l'oxyde de fer $\text{Fe}_2\text{O}_3\alpha$. *Materials Chemistry and Physics*. 1984;**10**:503-518. DOI: 10.1016/0254-0584(84)90001-4
- [28] Nakau T. Electrical conductivity of $\alpha\text{-Fe}_2\text{O}_3$. *Journal of the Physical Society of Japan*. 1960;**15**:727-727. DOI: 10.1143/JPSJ.15.727
- [29] Iordanova N, Dupuis M, Rosso KM. Charge transport in metal oxides: A theoretical study of hematite $\alpha\text{-Fe}_2\text{O}_3$. *Journal of Chemical Physics*. 2005;**122**:144305(1)-(10). DOI: 10.1063/1.1869492

- [30] Kwon J-H, Choi Y-H, Kim DH, Yang M, Jang J, Kim TW, Hong S-H, Kim M. Orientation relationship of polycrystalline Pd-doped SnO₂ thin film deposits on sapphire substrates. *Thin Solid Films*. 2008;**517**:550-553. DOI: 10.1016/j.tsf.2008.06.074
- [31] Ling Y, Wang G, Wheeler DA, Zhang JZ, Li Y. Sn-doped hematite nanostructures for photoelectrochemical water splitting. *Nano Letters*. 2011;**11**:211-2125. DOI: 10.1021/nl200708y
- [32] Koffyberg JP. Optical bandgaps and electron affinities of semiconducting Rh₂O₃(I) and Rh₂O₃(III). *Journal of Physics and Chemistry of Solids*. 1992;**53**:1285-1288. DOI: 10.1016/0022-3697(92)90247-B
- [33] Seki M, Yamahara H, Tabata H. Enhanced photocurrent in Rh-substituted α -Fe₂O₃ thin films grown by pulsed laser deposition. *Applied Physics Express*. 2012;**5**:115801(1)-(3). DOI: 10.1143/APEX.5.115801
- [34] Seki M, Takahashi M, Ohshima T, Yamahara H, Tabata H. Solid-liquid-type solar cell based on α -Fe₂O₃ heterostructures for solar energy harvesting. *Japanese Journal of Applied Physics*. 2014;**53**:05FA07(1)-(6). DOI: 10.7567/JJAP.53.05FA07
- [35] Mashiko H, Oshima T, Otomo A. Band-gap narrowing in α -(Cr_xFe_{1-x})₂O₃ solid-solution films. *Applied Physics Letters*. 2011;**99**:241904(1)-(3). DOI: 10.1063/1.3669704
- [36] Moore EA. First-principles study of the mixed oxide α -FeCrO₃. *Physical Review B*. 2007;**76**:195107(1)-(7). DOI: 10.1103/PhysRevB.76.195107
- [37] Uemoto K, Wentzcovitch RM. Effect of the d electrons on phase transitions in transition metal sesquioxides. *Physics and Chemistry of Minerals*. 2011;**38**:387-395. DOI: 10.1007/s00269-010-0412-1
- [38] Sartoretti CJ, Alexander BD, Solarska R, Rutkowska IA, Augustynski J, Cerny R. Photochemical oxidation of water at transparent ferric oxide film electrodes. *Journal of Physical Chemistry B*. 2005;**109**:13685-13692. DOI: 10.1021/jp051546g
- [39] Beatham N, Orchard AF, Thornton G. X-ray and UV photoelectron spectra of the metal sesquioxides. *Journal of Physics and Chemistry of Solids*. 1981;**42**:1051-1055. DOI: 10.1016/0022-3697(81)90129-3
- [40] Tang H, Matin MA, Wang H, Deutsh T, Al-Jassim M, Turner J, Yan Y. Synthesis and characterization of titanium-alloyed hematite thin film for photoelectrochemical water splitting. *Journal of Applied Physics*. 2011;**110**:123511(1)-(7). DOI: 10.1063/1/3671414
- [41] Temesghen W, Sherwood P. Analytical utility of valence band X-ray photoelectron spectroscopy of iron and its oxides, with spectral interpretation by cluster and band structure calculations. *Analytical and Bioanalytical Chemistry*. 2002;**373**:601-608. DOI: 10.1007/s00216-002-1362-3
- [42] Fujii T, Groot FMF, Sawatzky GA, Voogt FC, Hibma T, Okada K. In situ XPS analysis of various iron oxide films grown by NO₂-assisted molecular beam epitaxy. *Physical Review B*. 1999;**59**:3195-3202. DOI: 10.1103/PhysRevB.59.3195

- [43] McIntyre NS, Zetaruk DG. X-ray photoelectron spectroscopic studies of iron oxides. *Analytical Chemistry*. 1977;**49**:1521-1529. DOI: 10.1021/ac50019a016
- [44] Abe Y, Kato K, Kawamura M, Sakai K. Rhodium and rhodium oxide thin films characterized by XPS. *Surface Science Spectra*. 2001;**8**:117-125. DOI: 10.1116/11.20010801
- [45] Blomberg S, Lundgren E, Westerström R, Erdogan E, Martin NM, Mikkelsen A, Andersen JN. Structure of the Rh_2O_3 (0001) surface. *Surface Science*. 2012;**606**:1416-1421
- [46] Uekawa N, Kaneko K. Nonstoichiometric properties of nanoporous iron oxide films. *Journal of Physical Chemistry B*. 1998;**102**:8719-8724. DOI: 10.1021/jp982249x
- [47] Tossell JA, Vaughan DJ, Johnson KH. Electronic structure of ferric iron octahedrally coordinated to oxygen. *Nature Physical Science*. 1973;**244**:42-45. DOI: 10.1038/physci244042a0
- [48] Mizoguchi H, Hirano M, Fujitsu S, Takeuchi T, Ueda K, Hosono H. ZnRh_2O_4 : A p-type semiconducting oxide with a valence band composed of a low spin state of Rh^{3+} in a $4d^6$ configuration. *Applied Physics Letters*. 2002;**80**:1207-1209. DOI: 10.1063/1.1450252
- [49] Dekkers M, Rijnders G, Blank DHA. ZnIr_2O_4 , a p-type transparent oxide semiconductor in the class of spinel zinc- d^6 -transition metal oxide. *Applied Physics Letters*. 2007;**90**:021903(1)-(3). DOI: 10.1063/1.2431548
- [50] Lee YS, Lee JS, Noh TW, Byun DY, Yoo KS, Yamaura K, Takayama-Muromachi E. Systematic trends in the electronic structure parameters of the 4d transition-metal oxides SrMO_3 (M = Zr, Mo, Ru, and Rh). *Physical Review B*. 2003;**67**:113101(1)-(4). DOI: 10.1103/PhysRevB67.113101
- [51] Walter MG, Warren L, McKone JR, Boettcher SW, Mi Q, Santori EA, Lewis NS. Solar water splitting cells. *Chemical Reviews*. 2010;**110**:6446-6473. DOI: 10.1021/cr1002326

IntechOpen

